Homoclinic Points of 2-D and 4-D Maps via the Parametrization Method

Stavros Anastassiou[1], Tassos Bountis[1,2] and Arnd Bäcker[3,4]

[1]Center of Research and Applications of Nonlinear Systems (CRANS),
University of Patras, Department of Mathematics,
GR-26500 Rion, Greece
[2]Department of Mathematics,School of Science and Technology,
Nazarbayev University, Kabanbay-batyr, 53, 010000 Astana, Kazakhstan
[3]Technische Universität Dresden,
Institut für Theoretische Physik and Center for Dynamics, 01062 Dresden, Germany
[4]Max-Planck-Institut für Physik komplexer Systeme, Nöthnitzer Strasse 38,
01187 Dresden, Germany

E-mail: SAnastassiou@gmail.com

Abstract.

An interesting problem in solid state physics is to compute discrete breather solutions in $\mathcal{N}$ coupled 1–dimensional Hamiltonian particle chains and investigate the richness of their interactions. One way to do this is to compute the homoclinic intersections of invariant manifolds of a saddle point located at the origin of a class of $2\mathcal{N}$–dimensional invertible maps. In this paper we apply the parametrization method to express these manifolds analytically as series expansions and compute their intersections numerically to high precision. We first carry out this procedure for a 2–dimensional (2–D) family of generalized Hénon maps ($\mathcal{N} = 1$), prove the existence of a hyperbolic set in the non-dissipative case and show that it is directly connected to the existence of a homoclinic orbit at the origin. Introducing dissipation we demonstrate that a homoclinic tangency occurs beyond which the homoclinic intersection disappears. Proceeding to $\mathcal{N} = 2$, we use the same approach to accurately determine the homoclinic intersections of the invariant manifolds of a saddle point at the origin of a 4–D map consisting of two coupled 2–D cubic Hénon maps. For small values of the coupling we determine the homoclinic intersection, which ceases to exist once a certain amount of dissipation is present. We discuss an application of our results to the study of discrete breathers in two linearly coupled 1–dimensional particle chains with nearest–neighbor interactions and a Klein–Gordon on site potential.

1. Introduction

An important topic in the study of the dynamics of 1–dimensional lattices (or chains) of nonlinearly interacting particles is their ability to support under rather general conditions a very interesting type of localized oscillations called discrete breathers (see [31, Chpt. 7], [26]). These solutions simply execute periodic motion and involve one or more central particles that carry most of the energy, while all others in their immediate vicinity have amplitudes that vanish exponentially as the index of the particle n goes to $+\infty$ or $-\infty$. Take for example the so–called Klein-Gordon system of ordinary differential equations written in the form

$$\ddot{u}_n = -V'(u_n) + \alpha(u_{n+1} - 2u_n + u_{n-1}), \qquad V(x) = \frac{1}{2}Kx^2 + \frac{1}{4}x^4, \qquad (1)$$

where u_n for $-\infty < n < \infty$ is the amplitude of the n-th particle, $\alpha > 0$ is a parameter indicating the strength of coupling between nearest neighbors, and $V(x)$ is the on-site potential with primes denoting differentiation with respect to the argument of $V(x)$.

To construct such a discrete breather solution one may insert a Fourier series

$$u_n(t) = \sum_{k=-\infty}^{\infty} A_n(k)\exp(ik\omega_b t) \qquad (2)$$

in the equations of motion (1), where ω_b is the frequency of the breather. Setting the terms proportional to the same exponential equal to zero one obtains the system of equations

$$-k^2\omega_b^2 A_n(k) = \alpha(A_{n+1}(k) - 2A_n(k) + A_{n-1}(k)) - KA_n(k) - \sum_{k_1,k_2,k_3} A_n(k_1)A_n(k_2)A_n(k_3),$$
$$(3)$$

where $k_1 + k_2 + k_3 = k, \forall k, \ n \in \mathbb{Z}$. This equation defines an infinite-dimensional mapping in the space of Fourier coefficients $A_n(k)$. Time-periodicity is ensured by the Fourier basis functions $\exp(ik\omega_b t)$, while spatial localization requires that $A_n(k) \to 0$ exponentially as $|n| \to \infty$.

If we want to construct a breather solution one can start from its lowest order approximation by substituting $u_n(t) = 2A_n(1)\cos(\omega_b t)$ in (3) and obtain a 2–dimensional map for the largest coefficient $A_n(1) = A_n(-1) = A_n$ as follows

$$-\omega_b^2 A_n = \alpha(A_{n+1} - 2A_n + A_{n-1}) - KA_n - 3A_n^3, \qquad (4)$$

which may be written in the form

$$A_{n+1} = -A_{n-1} + \frac{1}{\alpha}\left(2 + K - \omega_b^2\right)A_n + \frac{3}{\alpha}A_n^3 . \qquad (5)$$

If we now define $x_n = A_n$ and $y_n = A_{n-1}$ the mapping (5) takes the 2–dimensional (2–D) form

$$x_{n+1} = -y_n + Cx_n + \frac{3}{\alpha}x_n^3, \qquad (6a)$$

$$y_{n+1} = x_n \qquad (6b)$$

where $C = (2 + K - \omega_b^2)/\alpha$. This mapping is area-preserving (and also symplectic) since the determinant of its Jacobian is unity for all x_n and y_n. The above approach has proved quite useful in the past and has led to a wide variety of interesting results concerning the computation and dynamics of breathers and multibreathers in a large family of 1–dimensional Hamiltonian lattices [14, 15, 16]. To our knowledge, such a study has not yet been carried out for coupled Hamiltonian chains of this type.

Breather solutions of the original chain (1) by definition must have large values of $|A_n|$ for small $n = 0, \pm 1, \pm 2, ...$, while $A_n \to 0$ as $n \to \pm\infty$. This implies that these amplitudes can be identified as homoclinic orbits lying at the intersections of stable and unstable manifolds of the origin, which if hyperbolic is necessarily a saddle point of the map (6). For any homoclinic intersection point, its orbit under forward (backward) iteration along the stable (unstable) manifold asymptotically converges to the origin. Thus the requirement that $A_n \to 0$ as $n \to \pm\infty$ is fulfilled at the outset. To locate such homoclinic orbits accurately, one must be able to write down precise expressions for the curves representing these manifolds and compute their points of intersection.

The purpose of this paper is twofold: First, we develop and apply the parametrization method to compute intersections of invariant stable and unstable manifolds of a certain class of 2–D and 4–D invertible maps. These are the types of maps used to obtain the largest coefficients A_n and B_n in the Fourier expansion of the n–th particle of two coupled chains. So far, such 2–D maps have been successfully used to obtain such A_n approximation for 1–D Hamiltonian particle chains with Klein-Gordon on-site potential (see [14, 15, 16, 17]). Second, we locate the coordinates of the homoclinic points of such mappings, along with the critical value of the dissipation parameter for which homoclinic intersections no longer exist. The accuracy of our computations of homoclinic points of 4–D maps is very encouraging, as an application of these techniques to coupled 1D particle chains is now possible.

The success of this approach in studying the existence of breathers relies on the fact that breather computation is achieved by using rapidly convergent Newton schemes to compute the breathers as simple periodic orbits of a Hamiltonian system of differential equations. As is well–known, this crucially relies on having an accurate first approximation. This is why the knowledge of the first Fourier coefficients from the homoclinic orbits of the corresponding maps is so useful. Indeed, higher Fourier coefficients are not needed, since they are obtained through the convergence of the Newton method to the exact breather solution.

The paper is structured as follows: First, in section 2, we introduce the 2–D mapping of interest here and prove its hyperbolic behavior for the symplectic case. In section 3 we explain the idea of the parametrization method and how we use it to obtain power series for the manifold equations. In section 4 we solve these equations numerically and obtain the homoclinic intersections for a cubic map of the form (6). Finally, in section 5, we apply our approach to a 4–D map with cubic nonlinearities and compute manifold intersections for various parameter values, commenting also on the accuracy limitations encountered by our numerical algorithms in this process. We close

with our concluding remarks in section 6.

2. Hyperbolicity in a Family of 2–Dimensional Hénon Maps

2.1. Generalized Hénon maps

Nearly 45 years ago the French astronomer Michel Hénon introduced a 2–D mapping of the plane onto itself with the simple form [2]

$$h : \mathbb{R}^2 \to \mathbb{R}^2, \ h(x,y) = (1 + y - ax^2, bx), \tag{7}$$

which exhibits very interesting phenomena related to chaos, bifurcations and strange attractors for different values of its parameters $a > 0$ and $|b| \leq 1$. In fact, the occurrence of some of the most important properties of (7) have been related to the transition from simple dynamics to hyperbolicity (see e.g. [4, 5, 12]). This implies that there are dense sets of chaotic orbits lying at the intersections of invariant manifolds of unstable (saddle) fixed points and periodic orbits [8].

Nowadays, however, it is more common to consider instead of (7) its conjugate expression

$$h_s : \mathbb{R}^2 \to \mathbb{R}^2, \ h(x,y) = (y, -bx + a - y^2), \tag{8}$$

which is more convenient to generalize both in form as well as number of dimensions, as described for example in [11] and [24]. Thus, let us consider the family of generalized Hénon maps of the plane onto itself defined by

$$H : \mathbb{R}^2 \to \mathbb{R}^2, \ H(x,y) = (y, -\delta x + p(y)), \tag{9}$$

where $p(y)$ is a univariate polynomial. This class is of particular importance as any polynomial mapping of the plane having a polynomial inverse (i.e. any member of the 2–D affine Cremona group) is either a composition of mappings of the form (9), or possesses trivial dynamics [6].

The main properties of the generalized Hénon family (9) are the following: First, the inverse of $H(x,y)$ is explicitly given as $H^{-1}(x,y) = (-\frac{1}{\delta}y + \frac{1}{\delta}p(x), x)$. Moreover, if the polynomial $p(y)$ is odd, the mapping $H(x,y)$ is symmetric under the transformation $\sigma(x,y) = (-x,-y)$, which implies $H \circ \sigma = \sigma \circ H(x,y)$. For $\delta = 1$ the mapping $H(x,y)$ is a symplectomorphism (or symplectic map), as it preserves the natural symplectic form of the plane, $\mathrm{d}x \wedge \mathrm{d}y$. In addition, H is also differentially conjugate to its inverse, since, if we define $\rho(x,y) = (y,x)$, it follows that $H \circ \rho = \rho \circ H^{-1}$ holds. As a consequence, in the symplectic case, invariant sets of $H(x,y)$ are related to invariant sets of H^{-1} by the transformation ρ.

Generalized Hénon maps have attracted a lot of attention in the literature. For example, in [13] the dynamics of $H(x,y)$ is studied, where $p(y)$ is a polynomial of third degree, while in [22] bifurcations of homoclinic tangencies are considered, involving intersections of invariant manifolds, for a mapping that has many similarities with (9)

above. Furthermore, we note that in [27] sufficient conditions are given for hyperbolicity in generalized Hénon maps for arbitrary polynomials $p(y)$.

In the present work we study a class of maps (9) that corresponds to the choice of a cubic polynomial $p(y)$ and generalize our results to the case of 4–D maps, as discussed in section 1 in connection with applications to discrete breathers in systems of 1–dimensional Hamiltonian particle chains [31, 14, 15, 16].

2.2. The 2–dimensional cubic map

Let us focus now on the dynamics of the recurrence relation:

$$A_{n+1} = cA_n - \delta A_{n-1} + 3A_n^3. \tag{10}$$

which follows from (5) by a simple rescaling of the Fourier coefficients, while a parameter $0 \leq \delta \leq 1$ has been introduced to account for dissipation effects. Setting $A_{n-1} = x$, $A_n = y$, we define the following cubic map of the plane x, y onto itself

$$f : \mathbb{R}^2 \to \mathbb{R}^2, \ (x, y) \mapsto (y, -\delta x + cy + 3y^3), \tag{11}$$

which corresponds to the generalized Hénon map (9) for $p(y) = cy + 3y^3$. Its inverse is given by

$$f^{-1}(x, y) = \left(\frac{c}{\delta}x - \frac{1}{\delta}y + \frac{3}{\delta}x^3, x \right). \tag{12}$$

For $\delta = 1$ the mapping f is a symplectomorphism and is invariant under the symmetry $\sigma(x, y) = (-x, -y)$, i.e. the relation $f \circ \sigma = \sigma \circ f$ holds.

2.3. Existence of a hyperbolic set in the symplectic case $\delta = 1$

The generalized Hénon map is known to have rich dynamics. In fact, in [27] the existence of hyperbolic sets for such maps has been proven for a wide range of parameter values.

2.1 Definition. Let $g : M \to M$ be a diffeomorphism and Λ a compact subset of M, invariant under this diffeomorphism. Λ is said to be a hyperbolic set for g if $\forall x \in \Lambda$ the following is true:

(i) $T_x M = E_x^\mathrm{s} \oplus E_x^\mathrm{u}$,

(ii) $d_x g(E_x^{\mathrm{s,u}}) = E_{g(x)}^{\mathrm{s,u}}$,

(iii) $\|d_x g|_{E_x^\mathrm{s}}\| < \lambda$, $\|d_x g^{-1}|_{E_x^\mathrm{u}}\| < \mu^{-1}$, for $0 < \lambda < 1 < \mu$.

These conditions imply that the tangent space of M at every point of Λ is the direct sum of two subspaces E_x^s and E_x^u which are invariant under the action of the differential of g. Moreover on these subspaces the differential acts as a contraction and dilation, respectively.

In what follows we will be interested in the diffeomorphism f defined by equation (11) for the particular choice of $c = -\frac{5}{2}$ which yields a saddle point at the

origin and will be kept fixed in the remainder of this paper. This choice is pictorially convenient, since c values in that range produce large scale manifolds that are clearly visible in the figures. Let us now demonstrate the existence of a hyperbolic set for this system:

2.2 Proposition. *Let f be the diffeomorphism* (11), *with $c = -\frac{5}{2}$ and $\delta = 1$. Then, there exists a hyperbolic set Λ on which f is topologically conjugate to the two–sided shift on three symbols. Moreover, Λ consists of all those points whose orbits are bounded under successive iterations of* (11).

Proof. The proof utilizes theorem 3.3 of [27]. However, since it is not directly applicable to f, we first perform a coordinate change by defining h_1, $h_2 : \mathbb{R}^2 \to \mathbb{R}^2$ as $h_1(x, y) = (\frac{1}{a}x, y)$ and $h_2(x, y) = (x, \frac{1}{a}y)$. Then, f is left–right equivalent to $\hat{f} : \mathbb{R}^2 \to \mathbb{R}^2$, defined by $\hat{f}(x, y) = (y, -\delta x + 3a^3 y^3 - \frac{5}{2}ay)$, that is, $h_1 \circ f = \hat{f} \circ h_2$. Note that this is nothing more than a coordinate transformation of both the domain of definition and the image of f, so, qualitatively, the behavior of f remains unchanged.

Let us now set $a = 5$ in this example. Following the notation used in [27], we notice that $\hat{f}$ is of the form $\hat{f}(x, y) = (y, -\delta x + p(y))$, where $p(y) = 375(y^3 - y/30) = 375g(y)$, with $g(y) = y^3 - y/30$. Determining the roots of $g(y)$ as $\alpha_1 = -1/\sqrt{30}$, $\alpha_2 = 0$, $\alpha_3 = 1/\sqrt{30}$, we consider the intervals $V_1 = (-1.03, -0.149)$, $V_2 = (-0.05, 0.05)$, $V_3 = (0.149, 1.03)$. Having thus chosen the neighborhoods of the map that are of interest, it is easy to verify that all conditions required for the application of Theorem 3.3 in [27] are satisfied, therefore the proposition holds. $\qquad\square$

Figure 1 shows the first few steps of the construction of the hyperbolic set for the above map $\hat{f}$.
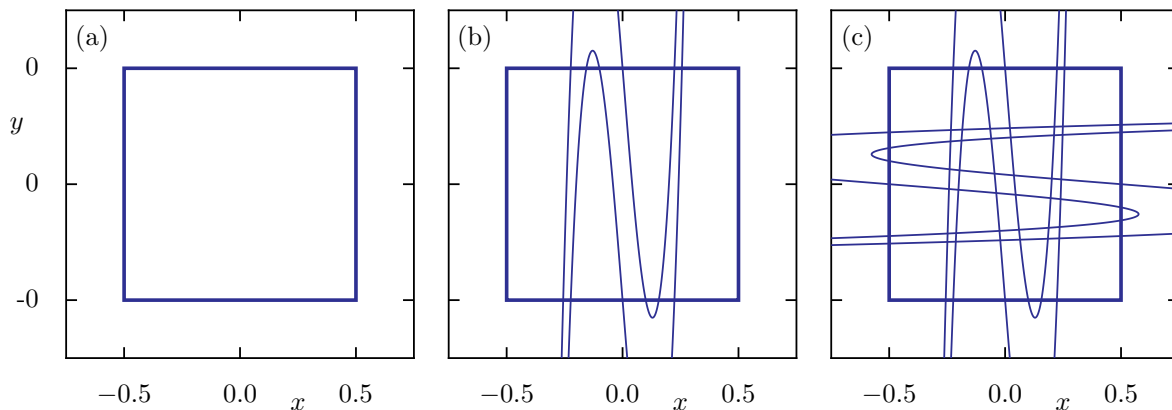

Figure 1. (a) The square $Q = [-1/2, 1/2] \times [-1/2, 1/2]$. (b) The area within the three vertical strips represents all points in the set $Q \cap \hat{f}(Q)$ generated after one forward iteration of all points of Q. (c) The points of Q that are still inside Q after one forward and one backward iteration of the map lie in the intersection of the vertical strips of (b) and the horizontal strips shown here. This set, $\hat{f}^{-1}(Q) \cap Q \cap \hat{f}(Q)$, represents the first step in the construction of the hyperbolic set of $\hat{f}$.

Hyperbolic sets persist for small perturbations of the mapping, thus we expect to find hyperbolic behavior of f for other values of δ as well. In later sections we show that the hyperbolic set established by the above proposition owes its existence to a transverse homoclinic point of f. Then we shall follow the intersections of the invariant manifolds of f emanating from the origin to locate the critical value $\delta_c < 1$ at which these manifolds are tangent to each other. This means that for $\delta < \delta_c$ homoclinic orbits no longer exist and the chaotic behavior of the map about the origin disappears [7]. To determine the invariant manifolds and compute their intersections, we make use of the so–called parametrization method, which we now briefly outline.

3. Overview of the Parametrization Method

Let $f : \mathbb{R}^n \to \mathbb{R}^n$ denote a C^∞ diffeomorphism, having a hyperbolic fixed point at $p \in \mathbb{R}^n$. Assume that E^s is the eigenspace of $d_p f : \mathbb{R}^n \to \mathbb{R}^n$, corresponding to eigenvalues that have norm less than one. The stable manifold theorem [3] asserts that the stable set of p, $W^s(p) := \{x \in \mathbb{R}^n \mid \lim_{n \to +\infty} f^n(x) = p\}$, is a smooth immersed submanifold of $\mathbb{R}^n$, tangent to E^s at p (an analogous statement holds for the unstable manifold of p).

Knowing how these two manifolds evolve in the phase space of the map offers crucial insight in the dynamics of the diffeomorphism f. Consequently, a number of methods have been developed to compute and visualize these manifolds. see [21] for a survey of these methods and more recently [29] for the 2–D case. Here we choose the parametrization method for the computation of such manifolds, which presents a number of advantages (see [20] for more details).

Let us now demonstrate how to compute stable (and unstable) invariant manifolds using the parametrization method. This method offers a simple and straightforward procedure for computing invariant manifolds of vector fields and diffeomorphisms as explained in detail in [18, 19, 20]. In fact, its applications go far beyond the topics we examine in this paper (see [23, 32, 33, 40, 28, 42] and references therein, for applications in a wide variety of problems).

The parametrization method builds on the following fact: Under the assumptions imposed on the diffeomorphism f, there exists a C^∞ injective immersion $S : E^s \to \mathbb{R}^n$, such that:
(a) $S(p) = p$,
(b) the derivative of S at p is the inclusion map $E^s \hookrightarrow \mathbb{R}^n$, and
(c) $f \circ S = S \circ f^s$, where f^s stands for the restriction of $d_p f$ to E^s.
This version of the stable manifold theorem may be found in [1], and the immersion S is to be thought of as the parametrization of $W^s(p)$, considered as a submanifold of $\mathbb{R}^n$.

Central to the implementation of the parametrization method is the equation

$$f \circ S = S \circ f^s, \tag{13}$$

which from now on we shall call the *defining equation* of the stable manifold. Here f stands for the diffeomorphism of interest, while f^s represents its linear part determined

by the stable eigenvalues of the fixed point. S denotes the parametrization of the invariant manifold that we wish to compute.

To proceed with this computation, we first need to expand the map S as a power series. Inserting this power series into the defining equation, we shall arrive at relations giving the coefficients of terms of degree n as a function of coefficients of terms of lower degree. What is especially convenient here is the fact that these relations are linear and are thus easily solved, provided all coefficients of lower order terms are given (for a specific application see section 4.1).

Making use of the facts (a) and (b) above, one immediately finds that the constant terms of the power series are none other than the coordinates of the fixed point p, while the coefficients of the linear terms are given by the eigenvectors of the stable eigenvalues. Thus, solving a set of linear equations as explained above, we may compute one by one the coefficients of our power series up to arbitrary (but finite) order. This series does indeed converge under mild assumptions on f, as explained in detail in [20].

In a completely analogous way the unstable manifold of p can also be computed. To accomplish this one simply has to replace f^{s} in the defining equation (13) by f^{u}, that is, the restriction of $d_p f$ onto the unstable subspace E^{u} of p. From here on, the procedure explained above is employed in precisely the same way to provide us with a parametrizion of the unstable manifold of p.

Let us now apply this technique to construct the invariant manifolds of the cubic 2–D diffeomorphism of interest here.

4. Invariant manifolds for the cubic diffeomorphism of the plane

Returning to the cubic mapping given in equation (11), let us note that it possesses three fixed points: The first one is the origin and exists for all parameter values, while there are also two symmetric ones, with coordinates $\left(\pm \frac{\sqrt{1-c+\delta}}{\sqrt{3}}, \pm \frac{\sqrt{1-c+\delta}}{\sqrt{3}} \right)$. Focusing at the $(0,0)$ fixed point, we first determine the eigenvalues of the linearized map

$$\frac{1}{2}\left(c - \sqrt{c^2 - 4\delta} \right), \ \frac{1}{2}\left(c + \sqrt{c^2 - 4\delta} \right), \tag{14}$$

and proceed to study its invariant manifolds, beginning with the $\delta = 1$ case and continuing with $\delta < 1$, where f becomes dissipative. Our purpose is to locate the homoclinic points which are part of the hyperbolic set of f. In fact, it suffices to locate the primary one at which the manifolds first meet, since it "generates", under repeated application of f and f^{-1}, all other points of the associated homoclinic orbit.

4.1 Definition. [9] Let $p \in W^{\mathrm{s}}(0,0) \cap W^{\mathrm{u}}(0,0)$, and denote by $S[(0,0),p]$ the segment of $W^{\mathrm{s}}(0,0)$ with endpoints $(0,0)$ and p and by $U[(0,0),p]$ the segment of $W^{\mathrm{u}}(0,0)$ with endpoints $(0,0)$ and p. The point p is called a primary (homoclinic) intersection (point) if $S[(0,0),p]$ intersects $U[(0,0),p]$ only at the points p and $(0,0)$.

As before, to fix ideas we set $c = -5/2$ and proceed in what follows with the computation of the primary intersection points for f, using the parametrization method.

4.1. The symplectic case $\delta = 1$

Since $c = -5/2$ and $\delta = 1$, the eigenvalues of the origin are $\lambda_u = -2$ and $\lambda_s = -1/2$ with normalized eigenvectors $(-1/\sqrt{5}, 2/\sqrt{5})$ and $(-2/\sqrt{5}, 1/\sqrt{5})$. The origin is therefore a saddle, with a 1–dimensional stable and a 1–dimensional unstable manifold, which we now proceed to determine.

Let $S^{\mathrm{u}} : \mathbb{R} \to \mathbb{R}^2$ be the parametrization of the unstable manifold emanating from the origin expressed by the expansion

$$S^{\mathrm{u}}(t) = \left(\sum_{n=0}^{+\infty} a_n t^n, \sum_{n=0}^{+\infty} b_n t^n \right). \tag{15}$$

The defining equation of this manifold becomes

$$f(S^{\mathrm{u}}(t)) = S^{\mathrm{u}}(\lambda_u t) \tag{16}$$

so that in the case of our 2–D map we obtain

$$\left(\begin{array}{c} \sum_{n=0}^{+\infty} b_n t^n \\ -\delta \sum_{n=0}^{+\infty} a_n t^n + c \sum_{n=0}^{+\infty} b_n t^n + 3 \left(\sum_{n=0}^{+\infty} b_n t^n \right)^3 \end{array} \right) = \left(\begin{array}{c} \sum_{n=0}^{+\infty} a_n \lambda_u^n t^n \\ \sum_{n=0}^{+\infty} b_n \lambda_u^n t^n \end{array} \right). \tag{17}$$

This gives, after equating terms of the same power of t, the following system

$$-\lambda_u^n a_n + b_n \qquad\qquad = 0 \tag{18a}$$

$$-\delta a_n + \left(c + 9b_0^2 - \lambda_u^n \right) b_n = s_{n-1}, \tag{18b}$$

where s_{n-1} is defined by

$$s_{n-1} := -3 \left(\sum_{j=1}^{n-1} b_0 b_{n-j} b_j + \sum_{i=1}^{n-1} \sum_{j=0}^{i} b_{n-i} b_{i-j} b_j \right). \tag{19}$$

The above is a linear system of equations for the coefficients a_n, b_n of the power series, whose zero-th order terms (a_0, b_0) are both zero since they represent the coordinates of the fixed point at the origin. The first order terms (a_1, b_1) on the other hand are simply the coordinates of the unstable eigenvector. Thus, we are now ready to compute the constants a_n, b_n for every, finite, value of $n > 1$.

To perform the numerical computation of $S^{\mathrm{u}}(t)$ we first truncate the series up to a polynomial $P^{\mathrm{u}}(t)$ of degree N which is evaluated using Horner's method. Still this polynomial will only be a good approximation of the unstable manifold for a restricted range of values of t. The range of validity can be quantified as follows:

4.2 Definition. Let $\varepsilon > 0$. Define $\tau > 0$ to be an ε-radius of validity of the polynomial approximation $P^{\mathrm{u}}(t)$ of $S^{\mathrm{u}}(t)$ if $\max_{t \in [-\tau, \tau]} ||f \circ P^{\mathrm{u}}(t) - P^{\mathrm{u}}(\lambda_u t)|| < \varepsilon$.
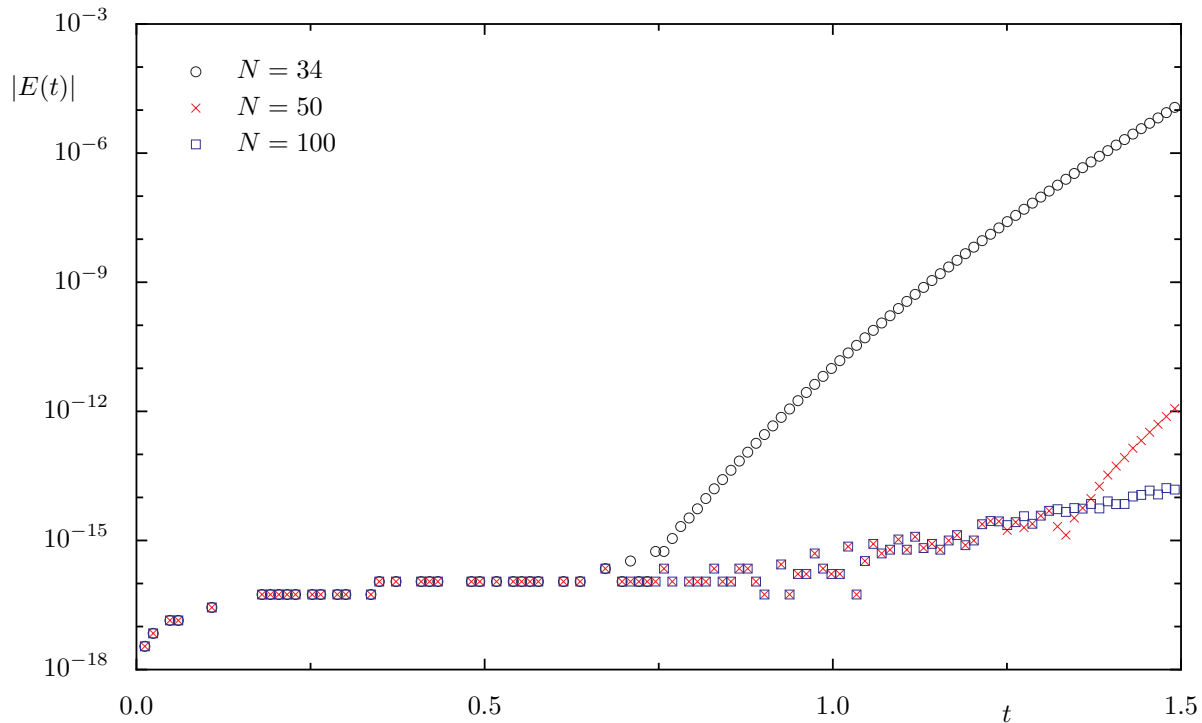
Figure 2. Plot of the error $E(t) = ||f \circ P^{\mathrm{u}}(t) - P^{\mathrm{u}}(\lambda_{\mathrm{u}} t)||$ for different degrees N of the polynomial for $\delta = 1.0$. This shows that with 100 coefficients and t up to 1.5 the error is below $2 \cdot 10^{-14}$.

Using this prescription, we shall keep terms up to order $N = 34$ of our series, for which we numerically obtain that $\tau = 0.75$ provides an ε-radius of validity, when we choose $\varepsilon = 10^{-15}$, see figure 2. For $t > \tau$ the error strongly increases. As also shown in this figure, increasing the order to $N = 100$ we can go as far as $\tau = 1.5$ for $\varepsilon = 2 \cdot 10^{-14}$, which turns out to be sufficient for accurately locating the primary (and all subsequent) homoclinic intersections, as explained below. Note, that in the definition of the error determining the ε-radius of validity, the difference between points at $\lambda_{\mathrm{u}} t$ is considered. Thus, for practical purposes we may assume that the parametrization method provides satisfactory results up to $\lambda_{\mathrm{u}} \tau$.

To obtain an equally good polynomial approximation $P^{\mathrm{s}}(t)$ for the stable manifold $W^{\mathrm{s}}(0,0)$ of the origin, we repeat the above steps, replacing λ_{u} with the stable eigenvalue λ_{s} in equation (16), and proceed to solve for the coefficients of the parametrization of the manifold. First, we replace the coefficients of the first order terms with the coordinates of the stable eigenvector. Actually, in the $\delta = 1$ case one may exploit the fact that f is differentially conjugate to its inverse under $\rho(x, y) = (y, x)$, and obtain its stable manifold as the image of its unstable manifold under ρ.

This symmetry is directly reflected in the coefficients of the polynomials of the parametrization method:

4.3 Lemma. Let $S^{\mathrm{u}}(t) = \left(\sum_{n=0}^{+\infty} a_n t^n, \sum_{n=0}^{+\infty} b_n t^n \right)$ be a parametrization of the unstable

manifold at the origin of the symplectomorphism f above. Then, a parametrization of the stable manifold of f at the origin is $S^{\mathrm{s}}(t) = \left(\sum_{n=0}^{+\infty} b_n t^n, \sum_{n=0}^{+\infty} a_n t^n\right)$.

Proof. Following from the system of equations (18) with $\delta = 1$ and $b_0 = 0$, the coefficients a_n, b_n of $S^{\mathrm{u}}(t)$ satisfy the following system of equations

$$- \lambda_{\mathrm{u}}^n a_n + b_n = 0 \tag{20}$$

$$- a_n + (c - \lambda_{\mathrm{u}}^n)b_n = -3 \sum_{i=1}^{n-1} \sum_{j=0}^{i} b_{n-i} b_{i-j} b_j, \tag{21}$$

Let us now suppose that $S^{\mathrm{s}}(t) = \left(\sum_{n=0}^{+\infty} C_n t^n, \sum_{n=0}^{+\infty} D_n t^n\right)$ represents the parametrization of the stable manifold of the origin. Note that, since f is a symplectomorphism, the stable eigenvalue λ_{s} equals $\lambda_{\mathrm{u}}^{-1}$. Clearly, the coefficients C_n, D_n satisfy the following system:

$$- \lambda_{\mathrm{s}}^n C_n + D_n = 0 \tag{22}$$

$$- C_n + (c - \lambda_{\mathrm{s}}^n)D_n = -3 \sum_{i=1}^{n-1} \sum_{j=0}^{i} D_{n-i} D_{i-j} D_j. \tag{23}$$

We claim that $C_n = b_n$, $D_n = a_n$. Indeed it follows from (22) that:

$$-\frac{1}{\lambda_{\mathrm{u}}^n} C_n + D_n = 0 \qquad \Leftrightarrow \qquad -\frac{1}{\lambda_{\mathrm{u}}^n} b_n + a_n = 0, \tag{24}$$

which is equivalent with (20), while from (23) we get

$$-C_n + (c - \lambda_{\mathrm{s}}^n)D_n = -3 \sum_{i=1}^{n-1} \sum_{j=0}^{i} D_{n-i} D_{i-j} D_j \tag{25a}$$

$$\Leftrightarrow \quad -C_n + \left(c - \frac{1}{\lambda_{\mathrm{u}}^n}\right)D_n = -3 \sum_{i=1}^{n-1} \sum_{j=0}^{i} D_{n-i} D_{i-j} D_j \tag{25b}$$

$$\Leftrightarrow \quad -b_n + \left(c - \frac{1}{\lambda_{\mathrm{u}}^n}\right)a_n = -3 \sum_{i=1}^{n-1} \sum_{j=0}^{i} a_{n-i} a_{i-j} a_j \tag{25c}$$

$$\Leftrightarrow \quad -b_n + \left(c - \frac{1}{\lambda_{\mathrm{u}}^n}\right)a_n = -3 \sum_{i=1}^{n-1} \sum_{j=0}^{i} \frac{1}{\lambda_{\mathrm{u}}^{n-i}} b_{n-i} \frac{1}{\lambda_{\mathrm{u}}^{i-j}} b_{i-j} \frac{1}{\lambda_{\mathrm{u}}^{j}} b_j \tag{25d}$$

$$\Leftrightarrow \quad -a_n + (c - \lambda_{\mathrm{u}}^n)b_n = -3 \sum_{i=1}^{n-1} \sum_{j=0}^{i} b_{n-i} b_{i-j} b_j, \tag{25e}$$

leading us back to (21). Thus, $C_n = b_n$ and $D_n = a_n$ as claimed. $\qquad \square$

So, either by solving the defining equation, or making use of Lemma 4.3, we arrive at a polynomial $P^{\mathrm{s}}(t)$ of degree $N = 34$, which is a satisfactory approximation of the stable manifold $S^{\mathrm{s}}(t)$, in the sense of Definition 4.2 and with the same radius of validity.
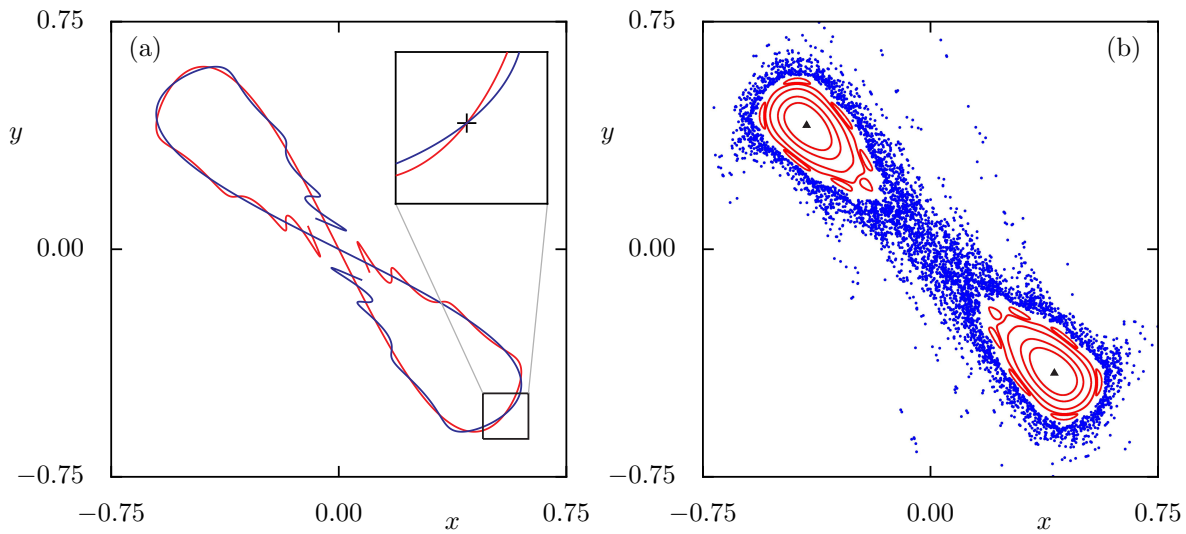
Figure 3. (a) Stable (blue) and unstable (red) manifolds computed using the parametrization method for $\delta = 1$. The inset shows a magnification around the primary homoclinic intersection at $(x^{\mathrm{h}}, y^{\mathrm{h}}) \approx (0.54527107, -0.54527107)$ which is indicated by a cross. (b) Regular orbits (red curves) around the periodic points of period 2 (black triangle) and several irregular orbits (blue dots) escaping via the homoclinic tangle.

Now, since the polynomial curve $P^{\mathrm{u}} : [-\tau, \tau] \to \mathbb{R}^2$ provides a good approximation of the local unstable manifold of the origin, we may iterate it using the mapping f to produce an approximation of the unstable manifold. The same holds for $P^{\mathrm{s}}(t)$, from which the corresponding stable manifold W^{s} can be obtained by iteratively applying f^{-1}.

Figure 3(a) shows the stable and unstable manifolds of the origin for $\delta = 1$. To obtain this plot, the parametrization method was used up to $t = t_{\max}$ with $t_{\max} = 0.42$. For example, for the unstable manifold, the segment obtained for $t \in [t_{\max}/\lambda_{\mathrm{u}}, t_{\max}]$ is iterated up to 6 times using f and then the corresponding segment of the stable manifold was obtained by symmetry. Note that, as the fixed point is inverse hyperbolic, one obtains alternatingly segments lying in the second and fourth quadrant.

Since a homoclinic point of transverse intersection between the stable and unstable manifolds exists, the Birkhoff-Smale theorem can be invoked to guarantee the existence of an infinity of transverse intersections, a phenomenon known as homoclinic chaos [8]. This explains the scattered points shown in the phase space of the mapping at $\delta = 1$, plotted in figure 3(b), where several orbits started in the region close to the hyperbolic fixed point at the origin eventually escape to infinity after a few iterations via the homoclinic tangle. Some elliptic periodic orbits as well as tori encircling the stable period–2 points in the 2nd and 4th quadrant are also shown.

4.2. Homoclinic intersections

We now wish to compute an approximation of the homoclinic intersection, i.e. the point $(x^{\mathrm{h}}, y^{\mathrm{h}})$ at which $W^{\mathrm{s}}(0,0)$ and $W^{\mathrm{u}}(0,0)$ intersect transversely. This means, that there are natural numbers $n_{\mathrm{u}}, n_{\mathrm{s}}$, along with $t_{\mathrm{u}}, t_{\mathrm{s}} \in \mathbb{R}$ such that $f^{n_{\mathrm{u}}}(P^{\mathrm{u}}(t_{\mathrm{u}})) = f^{-n_{\mathrm{s}}}(P^{\mathrm{s}}(t_{\mathrm{s}})) = (x^{\mathrm{h}}, y^{\mathrm{h}})$. Furthermore, since the intersection is transversal, the vectors $\frac{\partial}{\partial t_{\mathrm{u}}} f^{n_{\mathrm{u}}}(P^{\mathrm{u}}(t_{\mathrm{u}}))$ and $\frac{\partial}{\partial t_{\mathrm{s}}} f^{-n_{\mathrm{s}}}(P^{\mathrm{s}}(t_{\mathrm{s}}))$ are independent.

To evaluate such homoclinic points, we define the map $\Phi : \mathbb{R} \times \mathbb{R} \to \mathbb{R}^2$, as $\Phi(t_{\mathrm{u}}, t_{\mathrm{s}}) = f^{n_{\mathrm{u}}}(P^{\mathrm{u}}(t_{\mathrm{u}})) - f^{-n_{\mathrm{s}}}(P^{\mathrm{s}}(t_{\mathrm{s}}))$ and search for its zeros. One solution, of course, is the point $(t_{\mathrm{u}}, t_{\mathrm{s}}) = (0, 0)$ corresponding to the origin. Non–trivial roots $(t_{\mathrm{u}}, t_{\mathrm{s}})$ of this map for $(n_{\mathrm{u}}, n_{\mathrm{s}}) \in \mathbb{N} \times \mathbb{N}$ correspond to transverse homoclinic points of the mapping f. Validated computations can now be used to analytically prove the existence of such solutions for fixed parameter values, as described in [32, 40, 36]. Here however, we are more interested in accurately obtaining these solutions, while permitting the parameters to vary, until they no longer exist. Note that this is also the subject of reference [41], where the authors mention the possibility of applying the parametrization method, along with their technique, to obtain computer–assisted proofs of transversal intersections of manifolds. Here we proceed as described below.

To determine the homoclinic intersections for a sequence of decreasing values of δ it is convenient to start from an already computed homoclinic intersection at one δ value and use the corresponding $(t_{\mathrm{u}}, t_{\mathrm{s}})$ as a starting point for finding the solution of $\Phi(t_{\mathrm{u}}, t_{\mathrm{s}}) = (0, 0)$ for a slightly smaller δ. If no solution is found, the step size is reduced, so that effectively a bisection in δ is performed, approximating the critical value δ_{c} for which no homoclinics exist.

To determine the non–trivial roots of Φ it turns out to be particularly convenient to use polynomials of degree $N = 100$ as, under these circumstances, the range for $t_{\mathrm{u}}, t_{\mathrm{s}}$ can be extended to $[-1.6, 1.6]$ while the manifolds are still computed with sufficient accuracy, namely with $|E(t)| < 4 \cdot 10^{-14}$. Thus, we do not have to worry about the possibility of non-intersecting segments, noting also that segments of each manifold get mapped to the other quadrant across $(0, 0)$ due to the inverse hyperbolicity of the fixed point. For $\delta = 1.0$, for example, we obtain a zero of $\Phi(t_{\mathrm{u}}, t_{\mathrm{s}})$ for $(t_{\mathrm{u}}, t_{\mathrm{s}}) \approx (1.5849, -1.5849)$ and $n_{\mathrm{u}} = n_{\mathrm{s}} = 0$. This means that the manifolds can be represented up to the homoclinic point with high enough accuracy, using the parametrization method, while no additional application of the mapping f or its inverse is necessary. The corresponding homoclinic point is located at $(x^{\mathrm{h}}, y^{\mathrm{h}}) = (0.545271067753899, -0.545271067753900)$. The fact that both $t_{\mathrm{u}} + t_{\mathrm{s}} = 0$ and $x^{\mathrm{h}} + y^{\mathrm{h}} = 0$ within our numerical accuracy is already a good test of the quality of the numerically determined homoclinic point, particularly because the symmetry of the mapping for $\delta = 1.0$ has not been used in the computations.

To test the accuracy of the computed homoclinic intersection $(x^{\mathrm{h}}, y^{\mathrm{h}})$ we determine the distance d_n of $f^n(x^{\mathrm{h}}, y^{\mathrm{h}})$ from the origin for both positive and negative n. For positive n the iterates of the homoclinic point approach the origin along the stable manifold W^{s}, while, for negative n the approach is along the unstable manifold W^{u}.
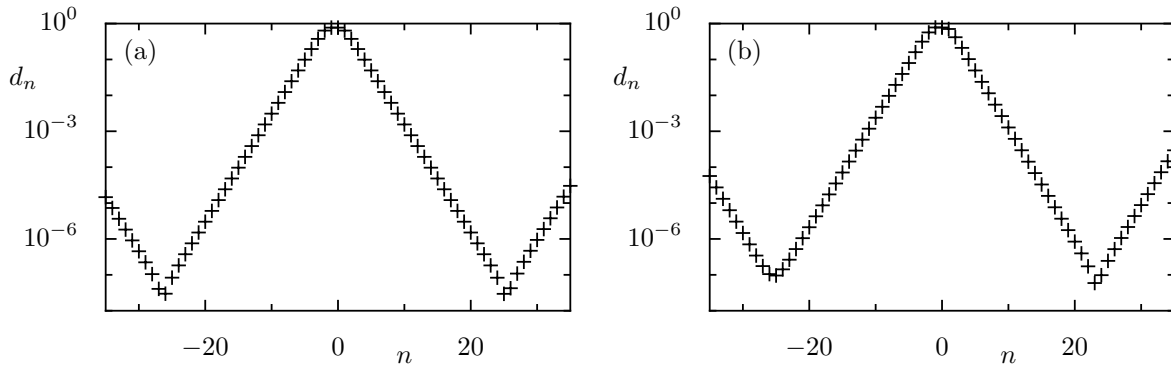
Figure 4. Plot of the distance d_n of the iterates $f^n(x^{\mathrm{h}}, y^{\mathrm{h}})$ from the origin. Note that the iterates of our computed homoclinic point $(x^{\mathrm{h}}, y^{\mathrm{h}})$ pass by the origin but stay away from it by an amount that provides a measure of the inaccuracy of the calculation. (a) $\delta = 1.0$ and (b) $\delta = 0.9714375$.

Any inaccuracy of the determined homoclinic intersection point (including additional round-off errors when applying f^n) implies that d_n eventually will increase again. This means that the inaccurate orbit will depart again from the origin along W^{u} for positive n and along W^{s} for negative n. The smallest distance to the origin thus gives a measure of the inaccuracy of the numerically determined homoclinic intersections, see figure 4(a) for $\delta = 1.0$ and (b) for $\delta < 1$.

So far we have relied on a graphical verification that the homoclinic intersection is actually transversal, i.e. that the vectors $\frac{\partial}{\partial t_{\mathrm{u}}} f^{n_{\mathrm{u}}}(P^{\mathrm{u}}(t_{\mathrm{u}}))$ and $\frac{\partial}{\partial t_{\mathrm{s}}} f^{-n_{\mathrm{s}}}(P^{\mathrm{s}}(t_{\mathrm{s}}))$ are independent. Due to the parametrization this can be easily checked by computing the determinant of the vectors $Df^{n_{\mathrm{u}}} \frac{\partial}{\partial t_{\mathrm{u}}} (P^{\mathrm{u}}(t_{\mathrm{u}}))$ and $Df^{-n_{\mathrm{s}}} \frac{\partial}{\partial t_{\mathrm{s}}} (P^{\mathrm{s}}(t_{\mathrm{s}}))$ for $n_{\mathrm{u}} = n_{\mathrm{s}} = 0$. This is shown in figure 5. With decreasing δ the determinant becomes smaller which means that the area spanned by the two tangent vectors becomes smaller and smaller until it becomes zeros at δ_{c}. The plot at figure 5 behaves like $\sqrt{\delta - \delta_{\mathrm{c}}}$. This suggests that at the critical parameter value δ_{c} the tangency of the stable and unstable manifolds is quadratic, which is a manifestation of the genericity of their intersection. A fit to $a\sqrt{\delta - \delta_{\mathrm{c}}}$ gives for the critical parameter $\delta_{\mathrm{c}} = 0.9713965579$.

4.3. Homoclinic tangency: the $\delta \simeq 0.971397$ case

Let us now follow the primary homoclinic intersection of the two manifolds as we decrease δ. Numerically we find a solution of $\Phi(t_{\mathrm{u}}, t_{\mathrm{s}}) = (0,0)$ as long as $\delta \in [\delta_{\mathrm{c}}, 1]$ with $\delta_{\mathrm{c}} = 0.971397$, meaning that below this δ_{c} homoclinic orbits no longer exist. Indeed, for $\delta < \delta_{\mathrm{c}}$ we do not obtain zeros of $\Phi(t_{\mathrm{u}}, t_{\mathrm{s}})$ with the required accuracy, i.e. components of $|\Phi(t_{\mathrm{u}}, t_{\mathrm{s}})|$ become larger than 10^{-15}. Figure 4(b) shows the corresponding distances d_n for $\delta = \delta_{\mathrm{c}}$ and demonstrates that the numerically determined homoclinic intersection is of comparable accuracy as in the case $\delta = 1.0$.

For the above mentioned value of $\delta = \delta_{\mathrm{c}}$ we compute the invariant manifolds using the parametrization method (followed by iterating the local manifolds). The result is
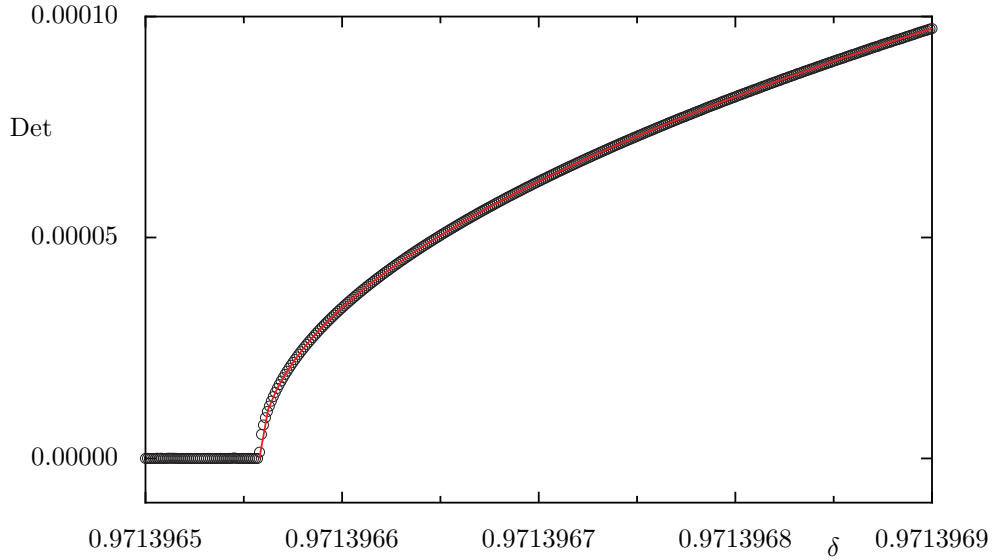
Figure 5. Plot of the determinant of the two vectors tangent to the stable and unstable manifolds at the homoclinic point, as a function of δ. The determinant is zero below the critical parameter value δ_c, while it tends to zero in a manner implying a quadratic tangency at this point. The red line is a fit to $a\sqrt{\delta - \delta_c}$.

shown in figure 6(a) and visually confirms that this is approximately the parameter at which the manifolds become tangent. For even smaller $\delta = 0.96$ one clearly finds that the stable and unstable manifold no longer intersect, as seen in figure 6(b).

We now turn our attention to linearly coupled 2–D mappings of the type studied above. Our objective is to calculate efficiently and accurately primary homoclinic orbits in the phase space of 4–D maps approximating breathers in coupled Hamiltonian chains.
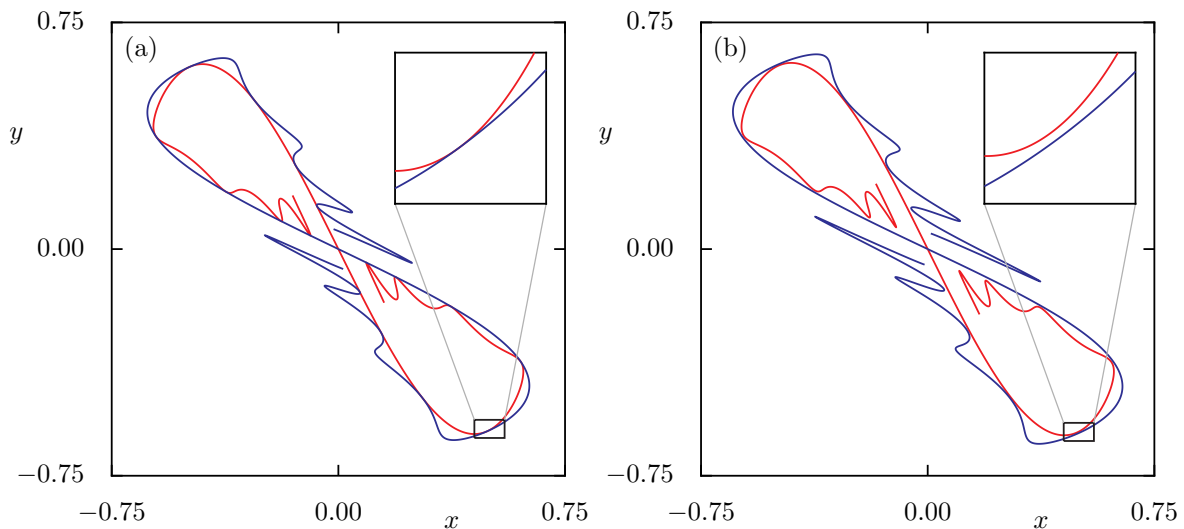
Figure 6. (a) Tangency of the stable and unstable manifolds shown at $\delta = 0.971397$. (b) For $\delta = 0.96$ the stable and unstable manifolds no longer intersect.

We wish to find out how computationally demanding is this task, and compare the results with analogous findings in the 2–D case.

5. Two coupled cubic systems

To investigate breather interactions in two linearly coupled chains of 1–dimensional Hamiltonian systems, the approach discussed in the introduction leads to the identification of homoclinic orbits of a 4–D map of the form:

$$A_{n+1} - cA_n + \delta A_{n-1} = 3A_n^3 + b(A_n - B_n) \tag{26a}$$

$$B_{n+1} - cB_n + \delta B_{n-1} = 3B_n^3 - b(A_n - B_n). \tag{26b}$$

where A_n and B_n are the leading terms of the Fourier coefficients corresponding to the discrete breathers in the first and second chain respectively. Setting $A_{n-1} = x_1$, $A_n = y_1$, $B_{n-1} = x_2$, $B_n = y_2$, we define the mapping $f : \mathbb{R}^4 \to \mathbb{R}^4$

$$f(x_1, y_1, x_2, y_2) = \begin{pmatrix} y_1 \\ cy_1 - \delta x_1 + 3y_1^3 + b(y_1 - y_2) \\ y_2 \\ cy_2 - \delta x_2 + 3y_2^3 - b(y_1 - y_2) \end{pmatrix}, \tag{27}$$

which is a diffeomorphism with inverse $f^{-1} : \mathbb{R}^4 \to \mathbb{R}^4$ given by

$$f^{-1}(x_1, y_1, x_2, y_2) = \begin{pmatrix} \frac{1}{\delta}((c+b)x_1 + 3x_1^3 - bx_2 - y_1) \\ x_1 \\ \frac{1}{\delta}((c+b)x_2 + 3x_2^3 - bx_1 - y_2) \\ x_2 \end{pmatrix}. \tag{28}$$

This map possesses a number of fixed points. However, we are only interested in the origin, which must be a saddle fixed point as in the 2–dimensional case. Thus, we choose parameter values for which the origin of the above 4–D map possesses a 2–dimensional stable manifold, and a 2–dimensional unstable manifold, corresponding to pairs of real eigenvalues with $|\lambda_{1,2}| > 1$ and $|\lambda_{3,4}| < 1$ respectively.

Let us suppose that $S^{\mathrm{u}} : \mathbb{R}^2 \to \mathbb{R}^4$ is the parametrization of the unstable manifold of the origin, corresponding to the eigenvalues λ_1, λ_2. If

$$S^{\mathrm{u}}(u, v) = \left(\sum_{n=0}^{+\infty} \sum_{m=0}^{+\infty} a_1^{nm} u^n v^m, \sum_{n=0}^{+\infty} \sum_{m=0}^{+\infty} a_2^{nm} u^n v^m, \sum_{n=0}^{+\infty} \sum_{m=0}^{+\infty} a_3^{nm} u^n v^m, \sum_{n=0}^{+\infty} \sum_{m=0}^{+\infty} a_4^{nm} u^n v^m \right) \tag{29}$$

represents its power–series expansion, where a_i^{nm}, $i \in \{1, 2, 3, 4\}$, are coefficients of the monomials $u^n v^m$, the defining equation of the manifold becomes

$$f \circ S^{\mathrm{u}}(u, v) = S^{\mathrm{u}}(\lambda_1 u, \lambda_2 v). \tag{30}$$

The left–hand side of this equation reads

$$
\begin{pmatrix}
\displaystyle\sum_{n,m} a_2^{nm} u^n v^m \\[2ex]
\displaystyle (c+b)\sum_{n,m} a_2^{nm} u^n v^m - \delta \sum_{n,m} a_1^{nm} u^n v^m + 3\left(\sum_{n,m} a_2^{nm} u^n v^m\right)^3 - b\sum_{n,m} a_4^{nm} u^n v^m \\[2ex]
\displaystyle\sum_{n,m} a_4^{nm} u^n v^m \\[2ex]
\displaystyle (c+b)\sum_{n,m} a_4^{nm} u^n v^m - \delta \sum_{n.m} a_3^{nm} u^n v^m + 3\left(\sum_{n,m} a_4^{nm} u^n v^m\right)^3 - b\sum_{n,m} a_2^{nm} u^n v^m
\end{pmatrix}
$$

while the right–hand side equals

$$
\begin{pmatrix}
\displaystyle\sum_{n,m} a_1^{nm} \lambda_1^n \lambda_2^m u^n v^m \\[2ex]
\displaystyle\sum_{n,m} a_2^{nm} \lambda_1^n \lambda_2^m u^n v^m \\[2ex]
\displaystyle\sum_{n,m} a_3^{nm} \lambda_1^n \lambda_2^m u^n v^m \\[2ex]
\displaystyle\sum_{n,m} a_4^{nm} \lambda_1^n \lambda_2^m u^n v^m
\end{pmatrix},
$$

where by $\sum_{n,m}$ we denote double summation over n and m ranging from 0 to ∞.

Equating now, as before, terms of the same degree, we arrive at the following system of equations for the coefficients

$$-\lambda_1^n \lambda_2^m a_1^{nm} + a_2^{nm} = 0, \tag{31a}$$

$$-\delta a_1^{nm} + (c+b - \lambda_1^n \lambda_2^m)a_2^{nm} - b a_4^{nm} = -3\sum_{k=0}^{n}\sum_{l=0}^{m}\sum_{i=0}^{k}\sum_{j=0}^{l} a_2^{n-k,m-l} a_2^{k-i,l-j} a_2^{i,j}, \tag{31b}$$

$$-\lambda_1^n \lambda_2^m a_3^{nm} + a_4^{nm} = 0, \tag{31c}$$

$$-b a_2^{nm} - \delta a_3^{nm} + (c+b - \lambda_1^n \lambda_2^m)a_4^{nm} = -3\sum_{k=0}^{n}\sum_{l=0}^{m}\sum_{i=0}^{k}\sum_{j=0}^{l} a_4^{n-k,m-l} a_4^{k-i,l-j} a_4^{i,j}. \tag{31d}$$

Note that the sums on the right side contain terms of the form a_i^{nm}, $i \in \{2,4\}$, as well. Although these terms should be isolated and transferred to the left side of the equations, we prefer to write them more "compactly" in the above form.

Cumbersome as they may seem, these equations are again linear with respect to the unknown a_i^{nm}, and may be solved immediately provided the terms of lower degree are known. The above equations will be crucially used in what follows to locate homoclinic points of the 4–D map f.

5.1. Error estimates for the parametrization of the manifolds

To study the 4–D map (27) we shall start from the uncoupled case $b = 0$, $\delta = 1$, and continue with the coupled case for small positive values of b. In this study, we
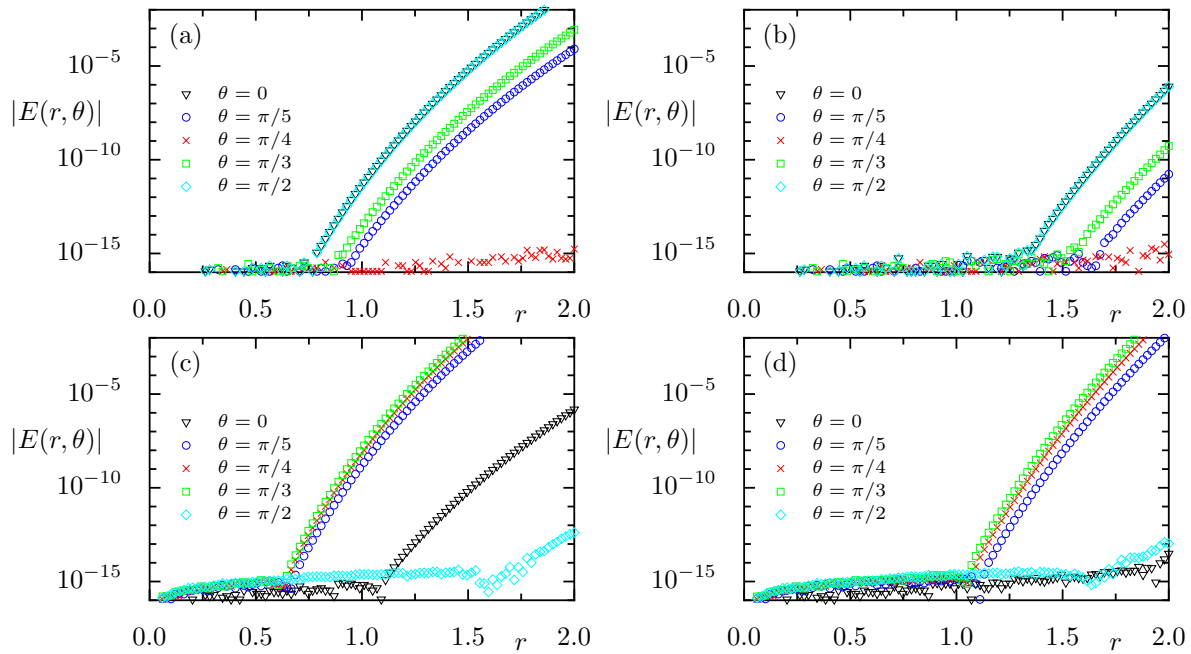
Figure 7. Evaluation of the error function $E(r,\theta)$ vs. r for the parametrization method for different values of θ and (a) $b = 0.0$, $N = 34$, (b) $b = 0.0$, $N = 50$, (c) $b = 0.1$, $N = 34$, and (d) $b = 0.1$, $N = 50$. Note how the accuracy of 10^{-15} extends to longer segments of the manifolds as N increases.

set $b = 0.1$ and continue the homoclinic intersections for $\delta < 1$ until they completely disappear. The question is whether these intersections persist as robustly as they do in the 2–dimensional case. To find out, we shall first consider an error estimate for the polynomial approximation of the series representing the (un)stable manifold.

Let us, therefore, define an analogous error function as in the 2–dimensional case

$$E : [-2, 2] \times [-2, 2] \to \mathbb{R}, \ E(u, v) = \|f \circ P^{\mathrm{u}}(u, v) - P^{\mathrm{u}}(\lambda_1 u, \lambda_2 v)\|, \qquad (32)$$

where P^{u} stands for the polynomial approximation of the unstable manifold, consider polar coordinates $(u, v) = (r\cos\theta, r\sin\theta)$ and plot $|E(r, \theta)|$ as a function of $r \in [0, 2]$, for various values of θ, see figure 7.

We first observe that, for all $b \in [0, 0.1]$, keeping terms up to order 50 in the polynomial representation P^{u} of the unstable manifold yields a region of validity with $r = 1$ corresponding to an error magnitude of order 10^{-15}. An analogous statement holds for the stable manifold as well. We thus keep the interval $r \in [0, 1]$ as the domain of definition of our approximations $P^{\mathrm{u}}(u_{\mathrm{u}}, v_{\mathrm{u}})$ and $P^{\mathrm{s}}(u_{\mathrm{s}}, v_{\mathrm{s}})$. Our aim is to locate non-trivial zeros of the mapping

$$\Phi(u_{\mathrm{u}}, v_{\mathrm{u}}, u_{\mathrm{s}}, v_{\mathrm{s}}) = f^{n_{\mathrm{u}}}(P^{\mathrm{u}}(u_{\mathrm{u}}, v_{\mathrm{u}})) - f^{-n_{\mathrm{s}}}(P^{\mathrm{s}}(u_{\mathrm{s}}, v_{\mathrm{s}})). \qquad (33)$$

Note, that as we will be using a sufficiently high order for the polynomials P^{u} and P^{s}, the homoclinic intersections already occur for values of $u_{\mathrm{u}}, v_{\mathrm{u}}, u_{\mathrm{s}}, v_{\mathrm{s}} < 1.16$ when using

$n_{\mathrm{u}} = n_{\mathrm{s}} = 0$. As in the 2–D case we assume that the parametrization method provides accurate results for this slightly extended range.

5.2. Homoclinic points for $b = 0$

For $b = 0$ our system reduces to two uncoupled 2–D maps of the form studied in previous sections. Thus the geometry in phase space is given by the direct product of two independent maps in (x_1, y_1) and (x_2, y_2). In each of these 2–D maps the origin is a fixed point and $(x^{\mathrm{e}}, y^{\mathrm{e}}) = (\pm 1/\sqrt{6}, \mp 1/\sqrt{6})$ are the coordinates of an elliptic periodic point of period 2. This implies that for $b = 0$ the 4–D map has: (i) The origin $(x_1, y_1, x_2, y_2) = (0, 0, 0, 0)$ as a hyperbolic-hyperbolic fixed point, (ii) two elliptic-hyperbolic period–2 orbits at $(x_1, y_1, x_2, y_2) = (\pm x^{\mathrm{e}}, \pm y^{\mathrm{e}}, 0, 0)$ and $(x_1, y_1, x_2, y_2) = (0, 0, \pm x^{\mathrm{e}}, \pm y^{\mathrm{e}})$, (iii) two elliptic-elliptic period–2 orbits, one at $(\pm x^{\mathrm{e}}, \pm y^{\mathrm{e}}, \pm x^{\mathrm{e}}, \pm y^{\mathrm{e}})$ and another at $(\pm x^{\mathrm{e}}, \pm y^{\mathrm{e}}, \mp y^{\mathrm{e}}, \mp y^{\mathrm{e}})$.

In order to visualize the regular dynamics occurring in the 4–dimensional phase space we use a 3–dimensional phase space slice [35]. As a convenient condition for
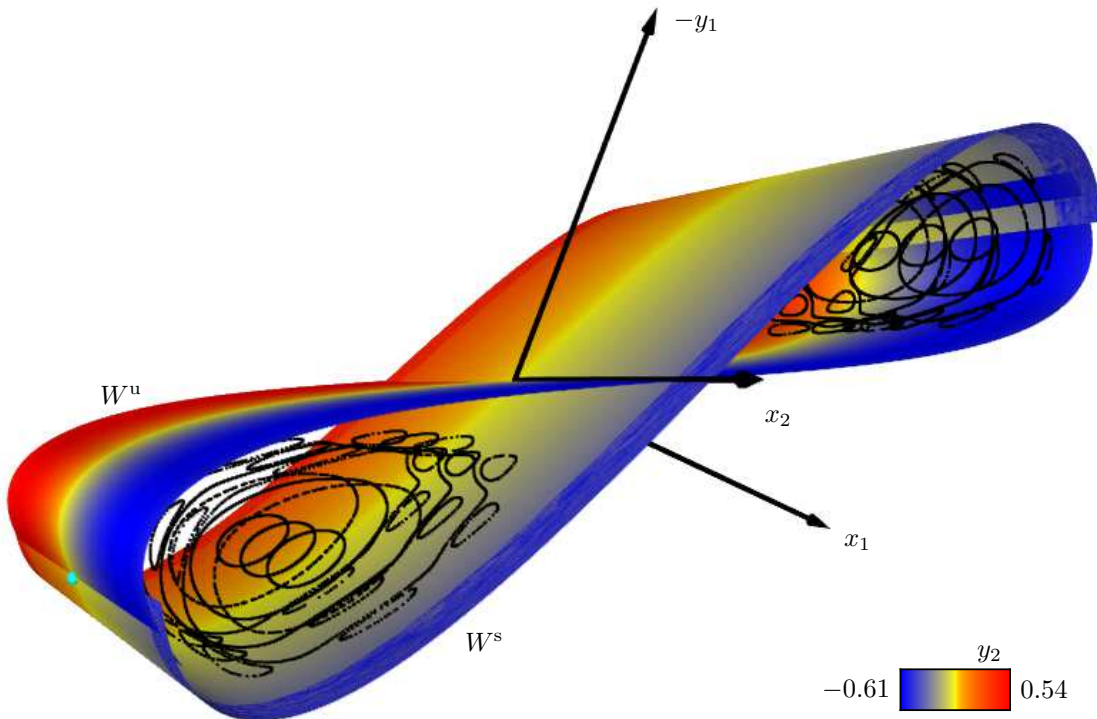

Figure 8. Homoclinic intersection shown by a small cyan sphere on the left part of the figure in the uncoupled case $b = 0$. Shown are the 2–dimensional stable and unstable manifolds as projections onto (x_1, x_2, y_1) space, with y_2 encoded in color. The black dots show some regular tori in a 3–dimensional phase space slice representation. For a rotating view see http://www.comp-phys.tu-dresden.de/supp/.

determining our slice we set $y_2^\star = y^{\text{e}}$, since it includes the domain surrounding one point of each elliptic-elliptic orbit of period 2. Whenever a point (x_1, y_1, x_2, y_2) of a trajectory fulfills the slice condition $|y_2 - y_2^\star| < 10^{-4}$ the remaining coordinates (x_1, y_1, x_2) are shown in a 3–D plot.

Figure 8 shows for the uncoupled case several regular orbits (black dots) surrounding the points of the elliptic-elliptic orbit of period 2. The 2–dimensional manifolds W^{s} and W^{u} have been computed using the parametrization method. They are embedded in the 4–dimensional phase-space and shown as projections onto (x_1, x_2, y_1). The projected coordinate y_2 is encoded in color. Thus a homoclinic intersection of W^{s} and W^{u} occurs at an intersection of the two surfaces, if and only if at the same point the color, i.e. the y_2 coordinate, also agrees. This point is indicated by a small cyan sphere on the left side of figure 8. In this case, the coordinates of the homoclinic points are given by $(x^{\text{h}}, y^{\text{h}}, 0, 0)$ and $(0, 0, x^{\text{h}}, y^{\text{h}})$, where $(x^{\text{h}}, y^{\text{h}})$ are the coordinates of the homoclinic point of the corresponding 2–D mapping studied in section 4.

5.3. Homoclinic points for $b > 0$

In order to determine the homoclinic intersection for different parameters b and δ we start from the uncoupled case $b = 0$, $\delta = 1$ and follow the homoclinic intersections with increasing b until $b = 0.1$. Numerically it is convenient to use the homoclinic intersection, described by the parameters $(u_{\text{u}}, v_{\text{u}}, u_{\text{s}}, v_{\text{s}})$, at one value of b as a starting point for finding the new root at a slightly different value for b. Subsequently, after we have found the homoclinic intersection at $b = 0.1$ with $\delta = 1$, we fix $b = 0.1$ and proceed to determine intersections at lower values of δ.

It turns out that the last intersection of the manifolds, at homoclinic tangency, occurs at about $\delta = 0.99601$, which is considerably larger (closer to the conservative case) than in the single 2–D map. To test the accuracy of our computations we again consider the distance d_n of $f^n(x_1^{\text{h}}, y_1^{\text{h}}, x_2^{\text{h}}, y_2^{\text{h}})$ from the origin for both positive and negative n, see figure 9, for $\delta = 0.997$. Interestingly enough, the magnitude of the observed minimal distance is comparable to the results for the 2–D case.

Analogously to the 2–D case, we calculated the determinant of the tangent vectors provided by the parametrization method at the homoclinic points, as a function of δ. Similarly to figure 5 the determinant approaches zero like $\sqrt{\delta - \delta_{\text{c}}}$, which is a manifestation of the quadratic tangency of the invariant manifolds for $\delta = \delta_{\text{c}}$.

Figure 10 shows a visualization of the two-dimensional manifolds W^{s} and W^{u} as projections onto (x_1, x_2, y_1) with y_2 encoded in color. The homoclinic intersection at $(x_1, y_1, x_2, y_2) = (0.46521450, -0.49858860, -0.08725131, 0.08972831)$ corresponds to an intersection of the manifolds in (x_1, x_2, y_1) and simultaneously in y_2, which means that the colors corresponding to the y_2 coordinate also agree. This point is indicated by a small cyan sphere at the left part of the figure. While both the above conditions hold for the example in figure 10, the illustration for $b = 0.1$ and $\delta = 0.99$ in figure 11 clearly shows that while the two manifolds intersect at several points in the projection
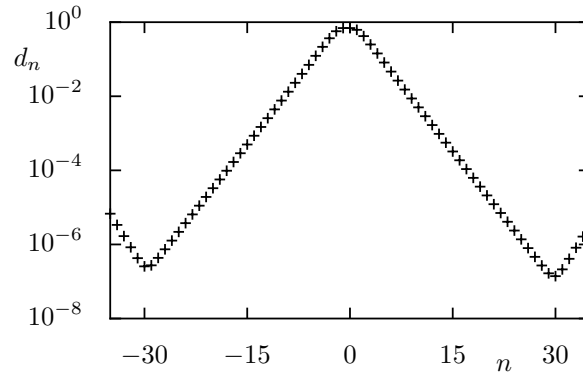
Figure 9. Plot of the distance d_n to the origin of iterates $f^n(x_1^{\mathrm{h}}, y_1^{\mathrm{h}}, x_2^{\mathrm{h}}, y_2^{\mathrm{h}})$ of numerically determined homoclinic intersection of the 4–D map for $b = 0.1$ and $\delta = 0.997$.

onto (x_1, x_2, y_1), the corresponding y_2 coordinates are different, as can be deduced from the different colors of the manifolds at their intersections in the projection. Thus the homoclinic intersection ceases to exist very quickly as δ decreases from 1 for fixed $b = 0.1$.

Note, that the parametrization method is not only numerically convenient to compute the homoclinic intersections of the 2–D manifolds, but also for their visualization. In contrast to computing the manifolds based on the linearized dynamics and application of the mapping, a simple two-dimensional uniform grid in the parametrization variables $(u_{\mathrm{u}}, v_{\mathrm{u}})$ and $(u_{\mathrm{s}}, v_{\mathrm{s}})$, respectively, leads to a well structured representation of the 2–D manifolds embedded in the 4–D phase space whose projection
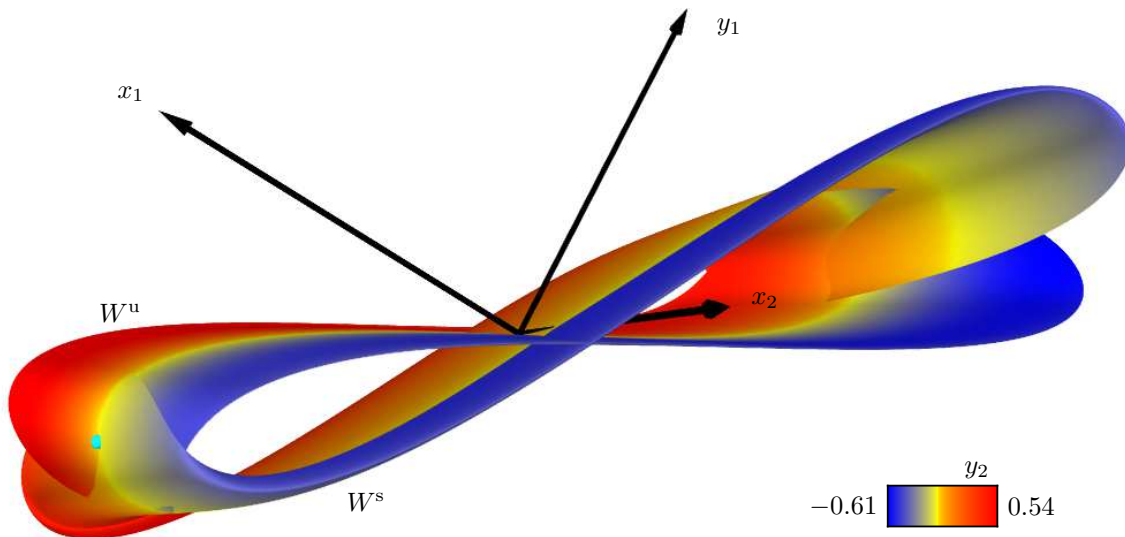
Figure 10. Stable and unstable manifolds computed using the parametrization method for the 4–D map for $b = 0.1$ and $\delta = 0.997$. A primary homoclinic intersection point is shown by a cyan sphere on the left side of the map. For a rotating view see http://www.comp-phys.tu-dresden.de/supp/.
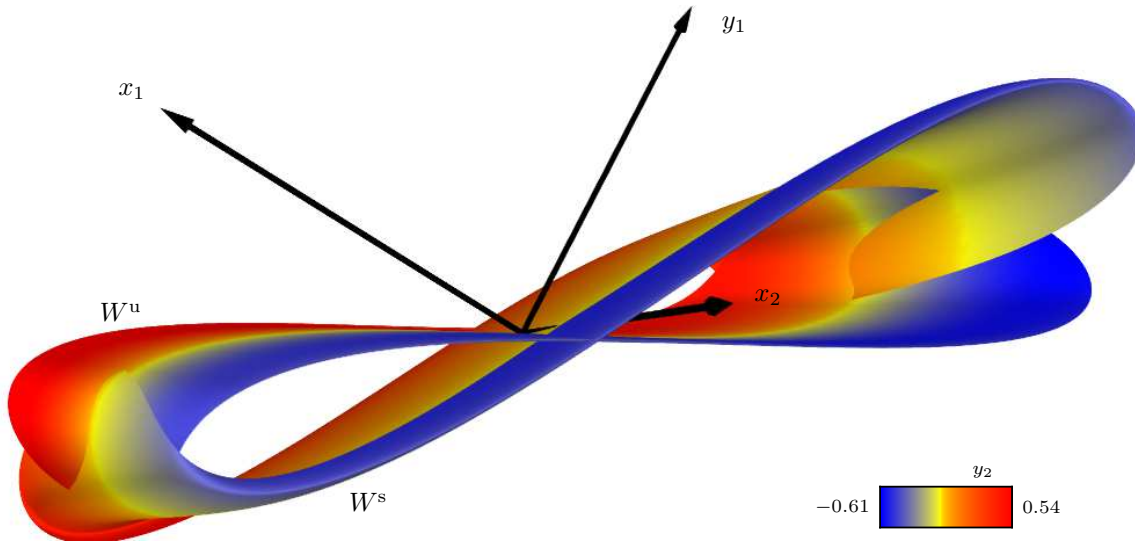
Figure 11. Stable and unstable manifolds computed using the parametrization method for the 4–D map for $b = 0.1$ and $\delta = 0.99$. No homoclinic intersection is found. For a rotating view see http://www.comp-phys.tu-dresden.de/supp/.

can be visualized in a straightforward way. Thus, for obtaining the manifolds shown in figures 8, 10, and 11 no further application of the map or its inverse is necessary. Note, however, that this would be required if we were to show more lobes, as for the used order of polynomials the approximation by the parametrization method is only accurate until a little beyond the homoclinic intersection.

6. Conclusions

In this paper we studied 2–D and 4–D polynomial maps arising in the approximate evaluation of the amplitudes of discrete breathers in single and double 1–dimensional Hamitonian lattices. We began with a 2–D map, which belongs to the generalized Hénon family, and computed its invariant manifolds using convergent series expansions derived by the parametrization method. We used parameter values at which tranversal intersections of the invariant manifolds of a saddle point at the origin are expected to occur, and followed these intersections until they disappeared by homoclinic tangency. Thus, we were able to verify independently the validity of these results by direct iteration, showing that at the identified parameters the points we were following cease to converge to the origin.

We then turned our attention to a 4–D map, obtained from two coupled 2–D maps of the previous form, resulting from two linearly coupled 1–dimensional Hamiltonian particle chains. Again we used the parametrization method to solve a system of linear equations and obtain the invariant manifolds of the saddle at the origin. Using continuation methods, we showed that despite the more complicated calculations, homoclinic orbits can be located without great difficulty and with comparable accuracy

as in the 2–D map case. The validity of our findings was checked again by finding parameter values at which homoclinic orbits disappear through a tangency of the corresponding manifolds. What is remarkable, both in the 2–D and in the 4–D case it was possible to accurately locate homoclinic points just using the parametrization method without any additional application of the mapping or its inverse.

Regarding other potential applications of our techniques, it would be very interesting to use them to approximate discrete breathers in coupled 1–dimensional Hamiltonian lattices, for which to our knowledge no results are available. Furthermore, the potential use of this approach to problems described by vector fields (and even p.d.e.'s) is worth exploring, in view of the effectiveness of the parametrization method in locating special solutions.

Moreover, higher–dimensional maps are interesting by themselves as they are known to arise in various physical applications like e.g. in the case of colliding particle beams of high energy accelerators, where the corresponding equations often appear in polynomial form (see e.g. [10, 25]). Recently, we have started looking into a number of potential applications of our methods to physical problems such as those mentioned above and results are expected in future publications.

Acknowledgements

References

[1] Smale S, "Dynamical systems and the topological conjugacy problem for diffeomorphisms", Proc.Inter.Cong.Math., Stockholm, Inst.Mittag–Leffler, 490-496, 1962.
[2] Hénon M, "A two–dimensional mapping with a strange attractor", Commun.Math.Phys., 50(1), 69-77,1976.
[3] Hirsch M W, Pugh C C and Shub M, "Invariant Manifolds", Springer, 1977.
[4] Devaney R and Nitecki Z, "Shift automorphisms in the Hénon mapping", Commun.Math.Phys., 67, 137-146, 1979.
[5] Franceschini V and Russo L, "Stable and unstable manifolds of the Hénon mapping", J.Stat.Physics, 25(4), 757-769, 1981.
[6] Friedland S and Milnor J,, "Dynamical properties of plane polynomial automorphisms", Erg.Th.Dyn.Systems, 9, 67-99, 1989.
[7] Glasser M L, Papageorgiou V G and Bountis T C, "Mel'nikov's Function for two-Dimensional Maps", SIAM J.Appl.Math., 49(3), 692-703, 1989.

[8] Wiggins S, "Introduction to Applied Dynamical Systems and Chaos", Springer–Verlag, New York, 1990.

[9] Wiggins S, "Chaotic Transport in Dynamical Systems", Springer, New York, 1992.

[10] Vrahatis M N, Isliker H and Bountis T C, "Structure and Breakdown of Invariant Tori in a 4-D Mapping Model of Accelerator Dynamics", Int.J.Bifurcation.Chaos, 7(12), 2707-2722, 1997.

[11] Lomelí H E and Meiss J D, "Quadratic volume preserving maps", Nonlinearity, 11(3), 557-574, 1998.

[12] Sterling D, Dullin H R and Meiss J D, "Homoclinic bifurcations for the Hénon map", Physica D, 134, 153–184, 1999.

[13] Dullin H R and Meiss J D, "Generalized Hénon maps: the cubic diffeomorphisms of the plane", Physica D, 143, 262-289, 2000.

[14] Bountis T, Capel H W, Kollmann M, Ross J C, Bergamin J M and van der Weele J P, "Multibreathers and homoclinic orbits in 1-dimensional lattices", Phys.Lett.A, 268, 50-60, 2000.

[15] Bergamin J M, Bountis T and Jung C, "A method for locating symmetric homoclinic orbits using symbolic dynamics", J.Phys.A, 33(45), 8059-8070, 2000.

[16] Bergamin J M, Bountis T and Vrahatis M, "Homoclinic orbits of invertible maps", Nonlinearity, 15(5), 1603-1619, 2002.

[17] Bergamin J M, "Numerical approximation of breathers in lattices with nearest neighbor interactions", Phys.Rev.E, 67, 026703, 2003.

[18] Cabré X, Fontich E, and de la Llave R, "The parameterization method for invariant manifolds I: Manifolds associated to non-resonant subspaces", Indiana Univ.Math.J., 52(2), 283-328, 2003.

[19] Cabré X, Fontich E, and de la Llave R, "The parameterization method for invariant manifolds II: Regularity with respect to parameters", Indiana Univ.Math.J., 52(2), 329-360, 2003.

[20] Cabré X, Fontich E, and de la Llave R, "The parameterization method for invariant manifolds III: Overview and applications", J.Diff.Eqs., 218(2), 444-515, 2005.

[21] Krauskopf B, Osinga H M, Doedel E J, Henderson M E, Guckenheimer J, Vladimirsky A, Dellnitz M and Junge O, "A survey of methods for computing (un)stable manifolds of vector fields", Int.J.Bifurcation.Chaos, 15(3), 763-791, 2005.

[22] Gonchenko V S, Kuznetsov Yu A and Meijer H G E, "Generalized Hénon map and bifurcations of homoclinic tangencies", SIAM J.Appl.Dyn.Systems, 4(2), 407-436, 2005.

[23] Haro A and de la Llave R, "A parameterization method for the computation of invariant tori and their whiskers in quasi-periodic maps: rigorous results", J.Diff.Eqs., 228(2), 530-579, 2006.

[24] Gonchenko S V, Meiss J D and Ovsannikov I I, "Chaotic Dynamics of three–dimensional Hénon maps that originate from a homoclinic bifurcation", Regul.Chaotic Dyn., 11(2), 191-212, 2006.

[25] Bountis T and Skokos Ch, "Space charges can significantly affect the dynamics of accelerator maps", Phys.Lett.A, 358(2), 126–133, 2006.

[26] Flach S and Gorbach A V, "Discrete breathers–Advances in Theory and Applications", Phys.Rep., 467, 1-116, 2008.

[27] Zhang X, "Hyperbolic invariant sets of the real generalized Hénon maps", Chaos, Solitons and Fractals, 43, 31-41, 2010.

[28] Mireles James J D and Lomelí H, "Computation of Heteroclinic Arcs with Application to the Volume Preserving Hénon Family", SIAM J.Appl.Dyn.Systems, 9(3), 919-953, 2010.

[29] Goodman R H and Wróbel J K, "High-order bisection method for computing invariant manifolds of two–dimensional maps", Int.J.Bifurcation.Chaos, 21, 2017-2042, 2011.

[30] Ramachandran P and Varoquaux G, "Mayavi: 3D visualization of scientific data", Comput.Sci.Eng., 13, 40–51, 2011.

[31] Bountis T and Skokos H, "Complex Hamiltonian Dynamics", Springer, Berlin, 2012.

[32] Mireles James J D and Mischaikov K, "Rigorous A Posteriori Computation of (Un)Stable Manifolds and Connecting Orbits for Analytic Maps", SIAM J.Appl.Dyn.Sys., 12(2), 957-1006, 2013.

[33] Mireles James J D, "Quadratic volume-preserving maps: (un)stable manifolds, hyperbolic dynamics, and vortex-bubble bifurcations", J.Nonlinear Sci., 23(4), 585-615, 2013.

[34] Efthymiopoulos C, Contopoulos G and Katsanikas M, "Analytical invariant manifolds near unstable points and the structure of chaos", Celest.Mech.Dyn.Astr., 119, 331–356, 2014.

[35] Richter M, Lange S, Bäcker A and Ketzmerick R, "Visualization and comparison of classical structures and quantum states of four-dimensional maps", Phys.Rev.E, 89, 022902, 2014.

[36] Mireles James J D, "Polynomial approximation of one parameter families of (un)stable manifolds with rigorous computer assisted error bounds", Indagationes Mathematicae, 26, 225–265, 2015.

[37] Contopoulos G and Harsoula M, "Convergence regions of the Moser normal forms and the structure of chaos", J.Phys.A, 48(33), 335101, 2015.

[38] Efthymiopoulos C, Harsoula M and Contopoulos G, "Resonant normal form and asymptotic normal form behaviour in magnetic bottle Hamiltonians", Nonlinearity, 28, 851–870, 2015.

[39] Delis N and Contopoulos G, "Analytical and numerical manifolds in a symplectic 4–D map", Celest.Mech.Dyn.Astr., 126, 313-337, 2016

[40] Haro À, Canadell M, Figueras J-L, Luque A, and Mondelo J M, "The Parameterization Method for Invariant Manifolds", volume 195 of "Applied Mathematical Sciences", Springer International Publishing, 2016.

[41] Capiński M J and Zgliczyński P, "Beyond the Melnikov method: A computer assisted approach", J.Diff.Equations, 262(1), 365-417, 2017.

[42] Capiński J and Mireles James J D, "Validated computation of heteroclinic sets", SIAM J.Appl.Dyn.Syst., 16(1), 375-409, 2017.